



Characterization of cold metal transfer and conventional short-circuit gas metal arc welding processes for depositing tungsten carbide-reinforced metal matrix composite overlays

Mohammad Reza Karimi¹ · Sheng-Hui Wang² · Jasmin Jelovica^{1,3}

Received: 12 May 2023 / Accepted: 14 July 2023 / Published online: 9 August 2023
© Crown 2023

Abstract

This paper compares the processing characteristics of advanced CMT (cold metal transfer) and conventional GMAW-S (gas metal arc welding with short-circuit metal transfer) processes for depositing Ni-WC MMC (nickel-based metal matrix composites reinforced with WC) overlays. In contrast to common expectations, advanced CMT technology with mechanically assisted droplet transfer could not demonstrate significant advantages over the GMAW-S process; on the contrary, CMT exhibits marginal disadvantages in terms of carbide transfer efficiency, volume fraction of retained WC, and deposition rate. Some carbides originally contained in the core of the feed wire are blown away and expelled out of the processing zone leading to physical losses of WC particles during the deposition processes, which is more significant for the CMT process owing to much higher waveform cycle frequency and cyclic feed wire retractions. CMT exhibits superior waveform stability, better control over penetration depth, marginally lower dilution level, and exceptional arc stability. The main parameters affecting carbide transfer efficiency and volume fraction of retained WC are wire feed speed and travel speed for both processes; increased wire feed speed and travel speed generally lead to decreased carbide transfer efficiency and reduced volume fraction of retained WC. Shielding gas may have different effects on the outcomes for the CMT and GMAW-S processes. CMT overlays show comparatively higher W and lower Fe concentration in the matrix, while GMAW-S overlays show a higher concentration of Fe in the matrix (due to elevated dilution level) with marginally higher matrix microhardness and more herringbone-like secondary carbide precipitates.

Keywords Cold metal transfer (CMT) · Gas metal arc welding (GMAW) · Ni-WC MMC · Physical loss of carbides · Carbide transfer efficiency · Carbide dissolution

1 Introduction

Nickel-based metal matrix composites reinforced with WC (Ni-WC MMC) provide robust protection for machinery and equipment operating in harsh environments such as mining,

extending the lifespan of production-critical components and minimizing maintenance expenses [1]. Thanks to the unique characteristics of WC, Ni-WC MMC overlays can not only improve wear properties but also enhance the corrosion resistance of the heavy-duty components [2]. The dissolution of WC particles into the molten matrix during the weld overlay process may negatively impact the wear resistance of the final product. Therefore, it is suggested to employ low-heat-input processes for the deposition to minimize the likelihood of thermally unstable WC particles dissolving in the molten matrix [3].

Gas metal arc welding (GMAW) is widely used for the hardfacing of large mobile mining equipment. Utilization of GMAW is driven by factors such as cost and efficiency, with a particular emphasis on productivity. Companies utilizing heavy haulers and related equipment are highly focused on sustained production. Therefore, manufacturers

✉ Sheng-Hui Wang
sheng-hui.wang@nrc-cnrc.gc.ca

¹ Department of Mechanical Engineering, The University of British Columbia, 6250 Applied Science Lane, Vancouver, BC V6T 1Z4, Canada

² Energy, Mining and Environment Research Centre, National Research Council of Canada, 4250 Wesbrook Mall, Vancouver, BC V6T 1W5, Canada

³ Department of Civil Engineering, The University of British Columbia, 6250 Applied Science Lane, Vancouver, BC V6T 1Z4, Canada

invest considerable effort to improve productivity to fulfill market demand and maintain market competitiveness [4]. Unfortunately, high WC dissolution is reported while using the GMAW process to deposit Ni-WC MMC overlays [3]. Günther et al. [5] quantified the effect of the GMAW process with short-circuit transfer (GMAW-S) and globular transfer mode on WC dissolution. They kept the dilution level fixed by regulating the amount of external hot wire introduced into the weld pool and demonstrated that the studied power range has minimal impact on WC dissolution. The study found that the globular transfer mode is responsible for up to 40% increase in WC dissolution compared to the short-circuit transfer mode, caused by higher process power and subsequently elevated droplet temperature.

As a new variant of GMAW, CMT process operates in short-circuit transfer mode, but it is integrated with sophisticated waveform control and reciprocating movement of feed wire (to facilitate the separation of the molten droplet from the tip of feed wire and its integration into the molten pool). This unique control offers improved arc stability and results in low-to-no spatter. Since Fronius International GmbH introduced CMT to the market in 2004, it has seen extensive use in a wide variety of welding applications, from welding aluminum [6, 7] to joining dissimilar materials [8, 9]. Additionally, CMT has gained significant attention from researchers and industry for its potential application in wire arc additive manufacturing due to its high production efficiency [10, 11].

According to Galeazzi et al. [12], however, wire arc additive manufactured samples deposited by CMT using AISI 420 wire did not show any significant improvement or difference in comparison to the standard GMAW, even though they observed higher arc stability of CMT over standard GMAW. These findings contradict the existing body of knowledge regarding CMT and conventional GMAW in literature. When it comes to the deposition of Ni-WC MMC overlays, the situation could be much more complicated, as tubular cored feed wire can cause challenges in achieving a stable arc [13] compared to solid feed wire.

Although conventional GMAW processes have been employed for depositing Ni-WC MMC overlays using tubular feed wires, few systematic studies have been reported to address associated excessive WC dissolution and low carbide transfer efficiency (η). As to the CMT process, there is even less work published regarding its use for the deposition of Ni-WC MMC overlays. In the authors' previous investigation [14], CMT process was successfully used for the deposition of single weld bead tracks of Ni-WC MMCs on steel plates; the process was optimized by using Taguchi's design of experiments (DOE), and the effects of processing parameters on f_{WC} , η and WC dissolution behavior were analyzed for the CMT process. Nonetheless, the frequently asked question, whether it is beneficial to use CMT for the

deposition of Ni-WC MMC overlays as compared to conventional GMAW processes, was not addressed there. To answer that question, this comparative study is to reveal the differences in the processing characteristics of CMT and GMAW-S for depositing Ni-WC MMC overlays. GMAW-S was chosen for the comparative study because it is believed to be a conventional low-heat GMAW process with dip-transfer mode, which offers the most similarities as compared to the advanced CMT process. Cladding test matrixes were designed by the Taguchi DOE to assess the processing characteristics.

2 Methodology

2.1 Materials

A36 hot rolled flat bar steel with the dimension of 100 mm × 75 mm × 10 mm was used as the substrate. A commercial tubular cored wire by COR-MET (with a nominal composition of NiCrBSi-55 wt.% WC and 1.6 mm diameter), COR[®]FACE 164M, was used as feed material [15]. The initial carbide volume fraction (f_p) of cored feed wire was calculated in our previous study [14] as 40.4%, representing the theoretical maximum amount of retained carbides that were achievable in the resultant overlays.

2.2 Experimental setup and design

The experimental setup is shown in Fig. 1. The welding system consists of two Fronius TransPuls Synergic 5000 power supplies equipped with two RCU 5000i remote control units, two VR 7000 CMT wire feeding units, and a Robacta Twin Compact Pro torch which is mounted on the tool flange of a

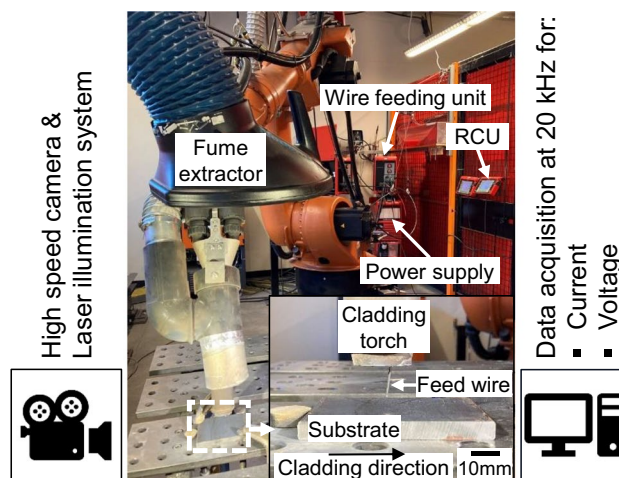


Fig. 1 Experimental setup including welding and robotic systems used in this study

6-axis KUKA robot. Single wire process was engaged for the cladding operations. Throughout all experiments, the contact tip-to-work distance was at 15 mm with the feed wire and the substrate angle set to 82°.

Single-track deposition of Ni-WC MMC overlays for a length of 50 mm was conducted using CMT (CrNi19 12 Cladding, ref. 1633) and GMAW (G3Si, ref. 744, and arc length correction of -15%) synergic modes programmed by the supplier. Taguchi’s design of experiment L16 orthogonal arrays were used to investigate the effects of processing parameters (WFS , travel speed (TS), and shielding gas (SG)) on f_{WC} , η , DL , deposition rate (DR), and weld bead geometry.

Table 1 is a summary of the test matrixes listing the welding control parameters for CMT and GMAW-S, respectively. The waveform characteristics of CMT (including wait current (I_w), short-circuit current (I_{sc}), boost current (I_b), and duration of boost phase (t_b)) and of GMAW-S (including arc current (I_{arc}) and arc voltage (V_{arc})) vary with changing WFS according to the selected synergic modes.

2.3 High-speed imaging

A monochromatic high-speed camera (Photron FASTCAM Mini AX100) at an acquisition rate of 2000 fps was used to visualize the deposition process. A bandpass filter of 808 nm, corresponding to the wavelength of the illuminating CAVILUX HF pulsed high-power diode laser, was used to reduce arc interference for the imaging process. These

images were also used to determine the length of the molten pool (the distance from the molten pool front to the end of the trailing liquid-to-solid boundary, as illustrated in Fig. 2). Finally, dwell time of WC particles was calculated using Eq. 1:

$$\text{Dwell time} = \frac{\text{Length of molten pool}}{\text{Cladding travel speed}} \tag{1}$$

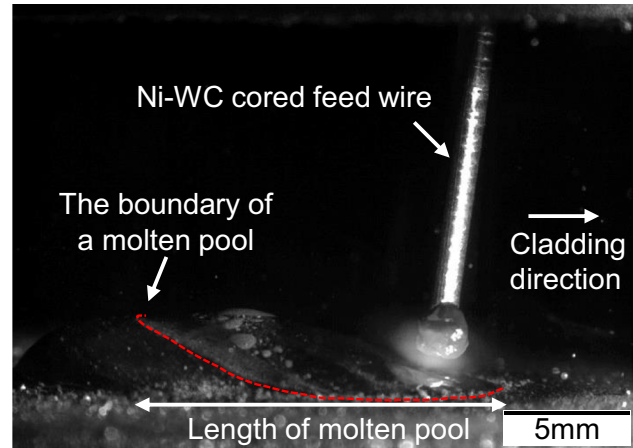


Fig. 2 Example of the boundary of a typical molten pool captured using the high-speed camera

Table 1 Cladding test matrixes including the processing parameters and the preset values for the waveforms of CMT and GMAW-S

Test Group	Test ID		WFS (m/min)	TS (m/min)	SG (% , Ar-balanced)	Preset values for CMT				Preset values for GMAW-S	
	CMT	GMAW-S				I_w (A)	I_{sc} (A)	I_b (A)	t_b (ms)	I_{arc} (A)	V_{arc} (V)
1	C1	G1	2.1	0.3	25% CO ₂	35	35	225	3	52.9	18.3
2	C2	G2		0.4	15% CO ₂						
3	C3	G3		0.5	2% O ₂						
4	C4	G4		0.6	5% O ₂						
5	C5	G5	3.9	0.3	15% CO ₂	60	40	290	3.75	103.9	19.5
6	C6	G6		0.4	25% CO ₂						
7	C7	G7		0.5	5% O ₂						
8	C8	G8		0.6	2% O ₂						
9	C9	G9	5.7	0.3	2% O ₂	82	73	307	5.13	147.9	21.3
10	C10	G10		0.4	5% O ₂						
11	C11	G11		0.5	25% CO ₂						
12	C12	G12		0.6	15% CO ₂						
13	C13	G13	7.5	0.3	5% O ₂	110	110	340	5.6	199.1	22.4
14	C14	G14		0.4	2% O ₂						
15	C15	G15		0.5	15% CO ₂						
16	C16	G16		0.6	25% CO ₂						

WFS wire feed speed, TS travel speed, SG shielding gas mixture, I_w wait current, I_{sc} short-circuit current, I_b boost current, t_b boost duration, I_{arc} arc current, V_{arc} arc voltage

2.4 Characterization of the overlays

To monitor the dynamics of welding waveforms, real-time measurements of the welding current and voltage were recorded at a sampling rate of 20 kHz. In cases where needed, the data recording was synchronized with a high-speed imaging process, by automatically trig-starting at the same time. Since there may be discrepancies between heat input calculated by traditional method (using average current and voltage) and instantaneous values, and since no single efficiency factor is universally accepted for the CMT process [16–18], average instantaneous power (*AIP*) is used to compare the arc power within various processing parameters, as determined by Eq. 2.

$$AIP \text{ (W)} = \frac{\sum_0^n (I_i \times V_i)}{n} \quad (2)$$

where I_i is a current sample, V_i is a voltage sample, n is the number of samples, and t is the sampling duration. For this evaluation, the time interval for the data recording is 0.05 ms.

The weight of each overlay sample was measured both before and after the deposition. The deposited weight was divided by the cladding time to obtain DR.

Microstructure evaluation of the overlays was carried out by cross-sectioning the samples at the first, middle, and third quarters along the cladding bead track, respectively. Samples were polished to a mirror surface and lightly etched by 2% Nital to reveal the interface of the overlays and the substrate. Cross-section images of the samples were taken by a KEYENCE VHX-7000 series digital microscope. These images were later used to calculate DL , f_{WC} , and η .

As shown in Fig. 3, cross-section images from the optical microscope were converted to binary images by ImageJ software. Interested regions were segmented to calculate f_{WC} , η , and DL using Eqs. 3–5, respectively. Please note that in the calculation of f_{WC} , both retained and primary WC are captured in image processing. However, the amount of primary WC, which are primary precipitates from dissolved carbides during the solidification process of the molten pools, is negligible compared to that of retained WC.

$$f_{WC} \text{ (\%)} = \frac{A_{WC}}{(A_R + A_P)} \quad (3)$$

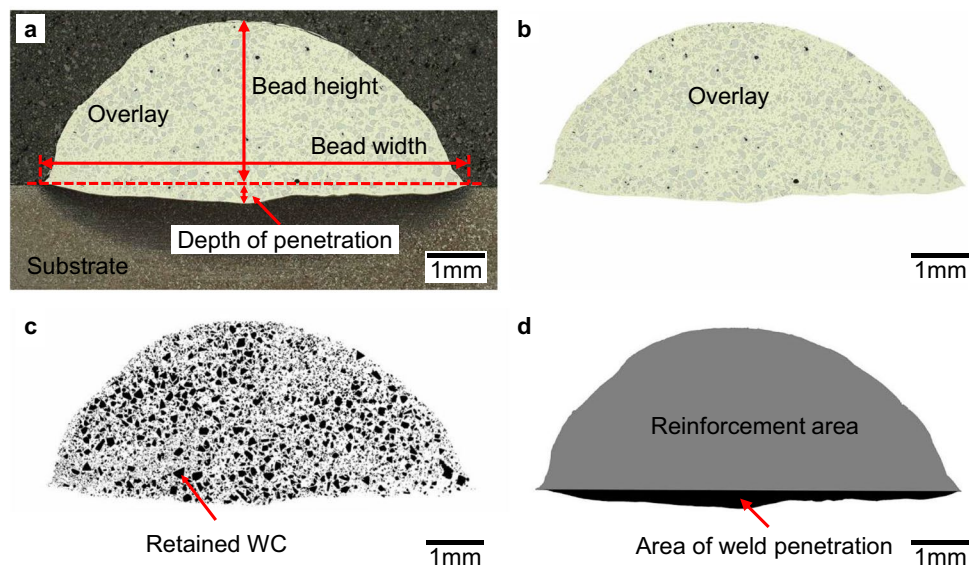
$$\eta \text{ (\%)} = \frac{A_{WC} / A_R}{f_P} \quad (4)$$

$$DL \text{ (\%)} = \frac{A_P}{(A_R + A_P)} \quad (5)$$

2.5 Microhardness

Vickers microhardness was performed on the selected samples in a vertical line through the entire cross-section using a Buehler 1600 series microhardness tester with a 500 g load, 15 s loading time, and indentation made every 0.25 mm. It should be noted that the indenter was positioned in a way to target indents on the matrix while avoiding landing on the large WC particles. Measurements were also performed on the substrate and Ni-sheath of the feed wire for reference purposes.

Fig. 3 An optical image of a typical overlay cross-section and the illustration of image processing for overlay characterization: **a** the original image of the overlay cross-section and related geometric parameters; **b** the extracted overlay; **c** the binary image of the overlay highlighting the segmented carbides; **d** the gray-scale image for dilution calculation



2.6 Weld bead geometry

The deposited samples were scanned with a 3D laser profile scanner perpendicular to the direction of the cladding direction, with 0.1 mm stepover and 0.01 mm resolution. The scanned results were subsequently processed using MATLAB to determine bead geometry by fitting a polynomial curve to the bead profile, achieving a minimum R^2 of 0.9 across all samples. The reported values for W , H , W/H , and A_R are the average of the scanned data throughout the entire length of the overlay bead by discarding the irregularity at the beginning and end of the bead track, as shown in Fig. 4.

3 Results and discussion

3.1 Waveform analysis

Current and voltage waveforms are indicators of the arc stability and comprise three main parts: a cyclical portion stemming from the current pattern, a transient element originating from recurring processes during welding (such as droplet detachment, arc ignition and extinguishing, and short circuiting), and noise signals generated by arc disruptions, such as arc blow, shielding gas flow disturbance, and spatters [19]. In the following subsections, cyclograms and dynamic characterization of the waveforms will be discussed to evaluate the stability of the CMT and GMAW-S processes.

3.1.1 Cyclogram examination

A cyclogram represents the cyclic variation of voltage and current in a welding process, providing a qualitative assessment of the processing stability by showcasing distinct phases. Figures 5 and 6 illustrate the cyclograms for the CMT and GMAW-S tests, respectively.

Cyclogram data follows a counterclockwise oscillation, where the density distribution of points serves as an effective means to differentiate various phases of a process and their stability. For the CMT process, the boost, wait, and short-circuit phases can be recognized by pinpointing areas with a higher density distribution. The overall elliptical shape of cyclograms for CMT samples stays consistent across various control parameters, while the area expands as WFS increases which correlates to an enlarged range of processing current and voltage. The position of high-density points shifts with higher WFS along the x -coordinate (current), while their location along the y -coordinate (voltage) remains relatively stable. Furthermore, at a constant WFS , TS does not significantly alter the shape or size of cyclograms; however, O_2 -containing SG appears to have a smaller cyclogram periphery, indicative of greater stability [20].

For the GMAW-S tests, cyclograms exhibit more dispersion and increased noise data, implying a lack of regularity and occurrences of unstable events. As WFS increases, cyclograms shift along the x -coordinate toward higher current values. Similar to the CMT tests, there are no significant

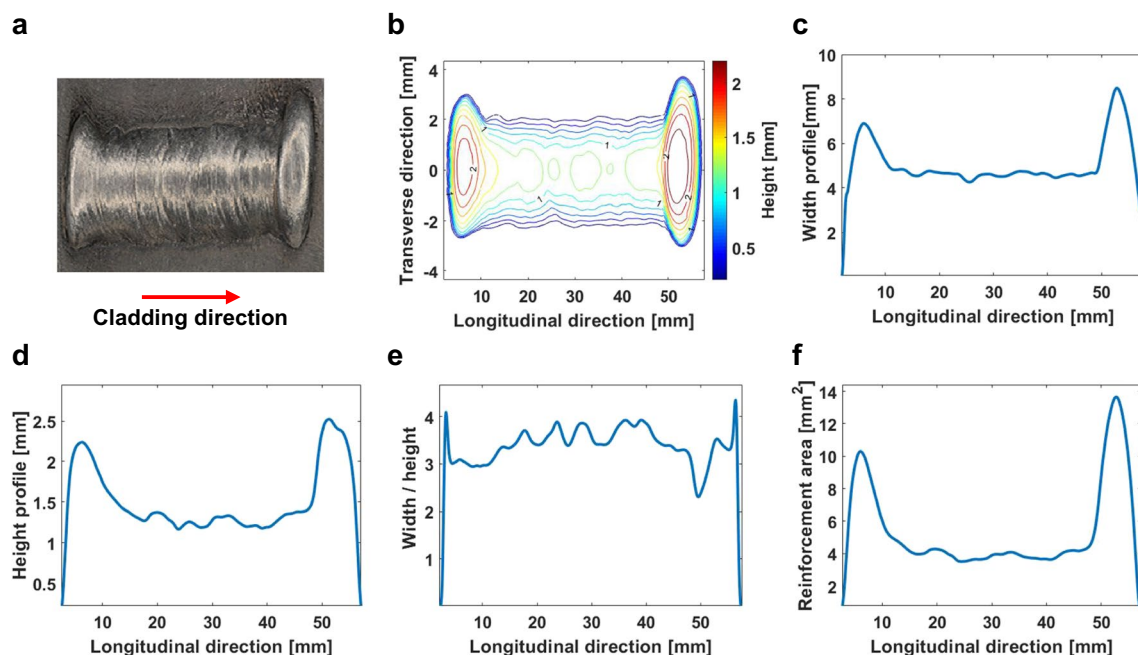


Fig. 4 Geometric characterization of a weld bead by a 3D laser profile scanner: **a** original optical top-view image of the deposited weld bead (with aspect ratio matched to the digital 2D contour plot); **b** fit-

ted digital 2D contour plot; **c** bead width profile; **d** bead height profile; **e** bead width-to-height ratio; **f** bead reinforcement area

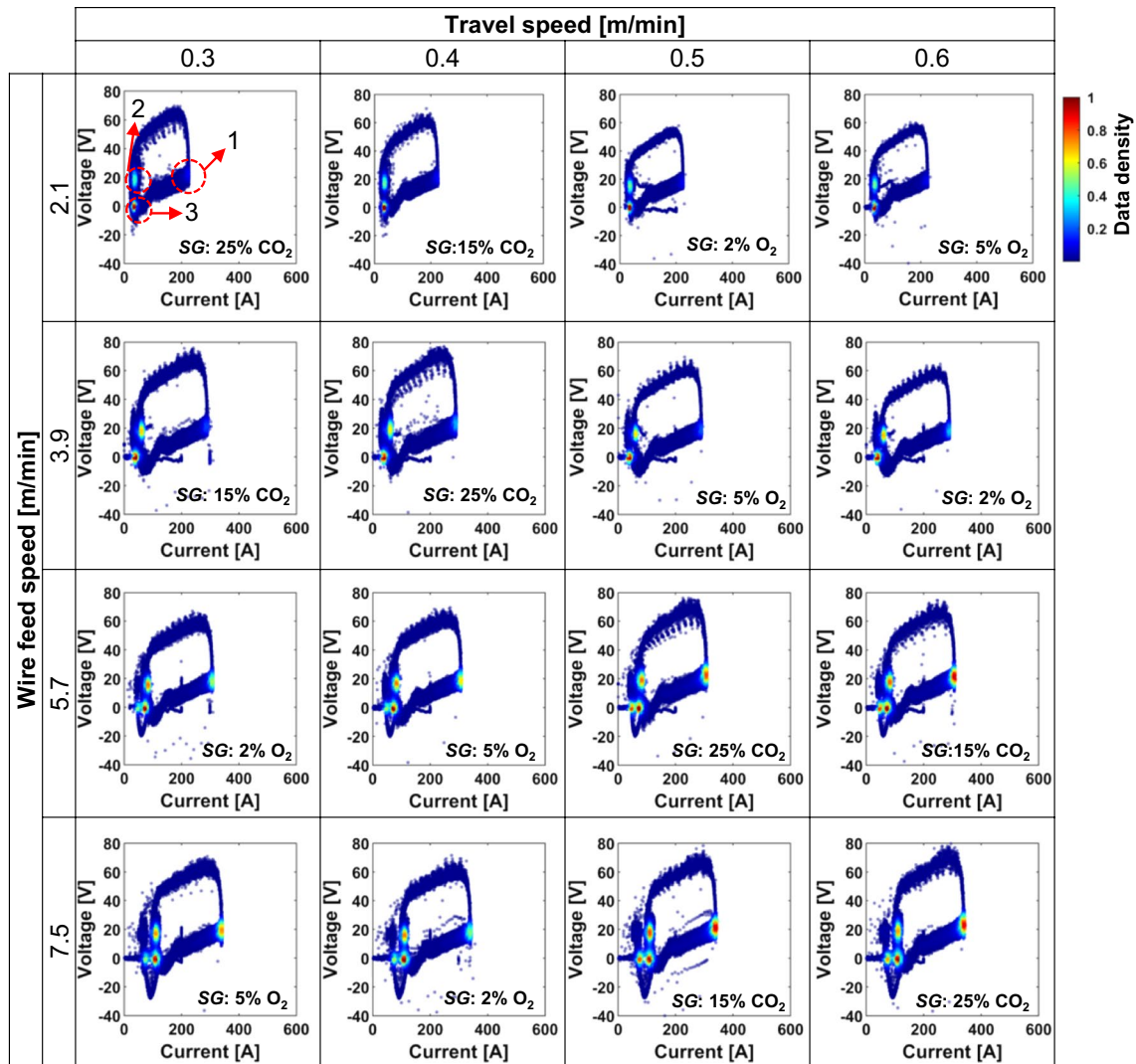


Fig. 5 Cyclograms (current-voltage waveforms) for CMT tests (1: boost phase; 2: wait phase; 3: short-circuit phase)

shifts along the y -coordinate (voltage) for high-density points. Additionally, it appears that a SG mixture containing 25% CO_2 extends the periphery along the horizontal direction (i.e., x -coordinate), indicating reduced stability.

3.1.2 Waveform comparison

Typical waveforms for the CMT and GMAW-S processes with comparable processing parameters are shown in Fig. 7. High-speed camera images are also presented, to demonstrate the characteristics of arcing and/or droplet forming/transfer at different moments of the waveform cycle. CMT cycle consists of two main phases: short-circuit and arcing ones. The arcing phase is further divided into the boost and wait phases. During the boost phase, the current quickly rises, reigniting the arc between the electrode and substrate, causing droplet formation at the electrode tip. The wait phase follows the

boost phase; as the electrode moves toward the weld pool, the current decreases to prevent the globular transfer of the droplet, and the voltage changes (based on the selected program) to maintain the arc intensity. When the molten droplet gets in touch with the weld pool (initiating the short-circuit phase), the current starts to drop sharply, and the electrode retracts, facilitating the detachment of the molten droplet from the tip of the feed wire and its transfer into the weld pool. The duration of the short-circuit phase cannot be adjusted once a CMT synergic mode has been chosen [21].

The GMAW-S cycle includes short-circuit and arcing phases. The short-circuit phase begins with the molten droplet touching the welding pool (forming a metallic bridge), which is reflected by a sudden increase in the current and a rapid drop in voltage. This current increase leads to a reduced conduction area and intensifies the pinch force, leading to the droplet detachment from the tip of the

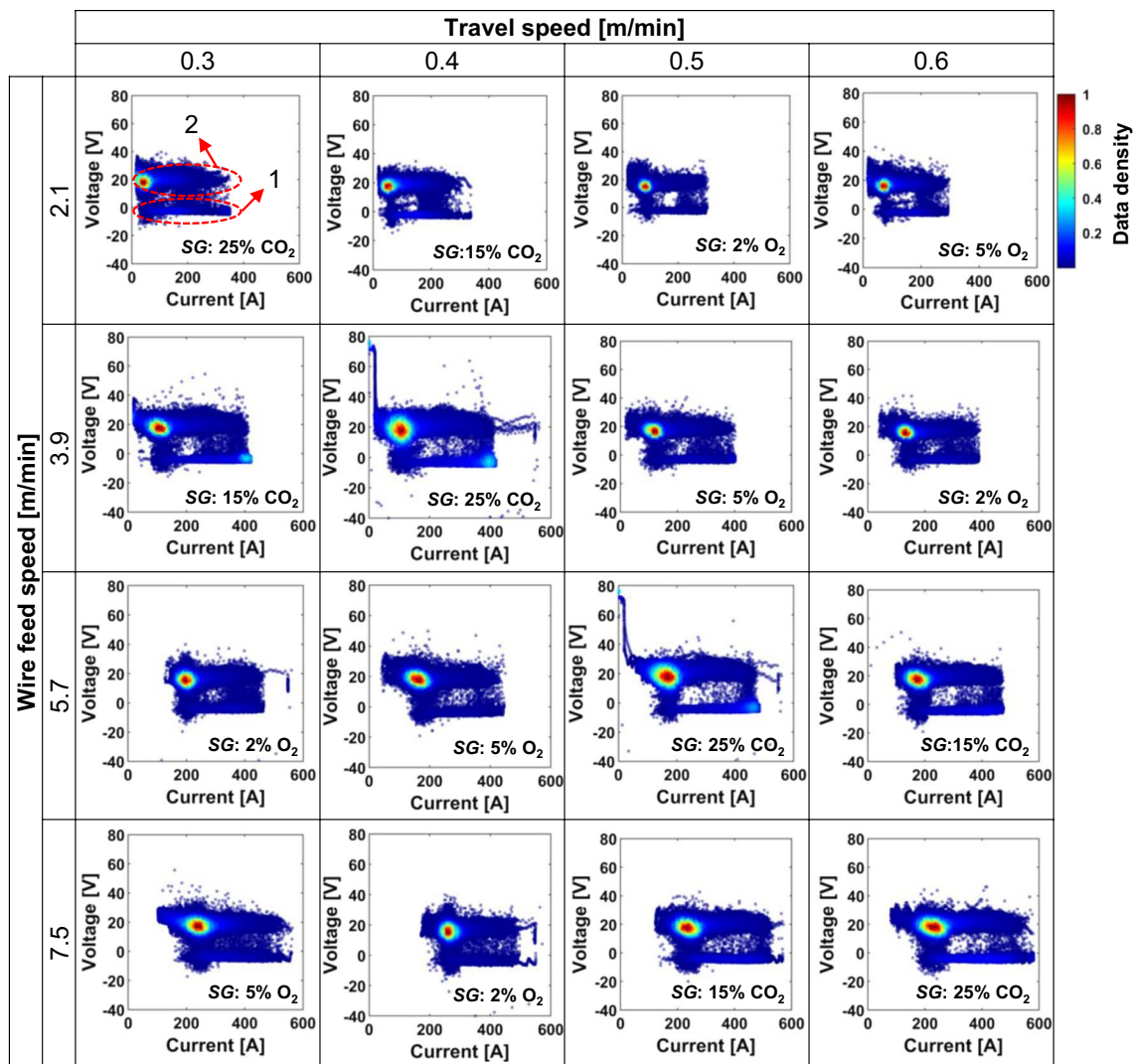


Fig. 6 Cyclograms (current-voltage waveforms) for GMAW-S tests (1: short-circuit phase; 2: arcing phase)

feed wire at the peak of the current spike and the rupture of the metal bridge. Thereafter, the arcing phase restarts and the arc reignites, while the current drops and the voltage increases to the preset value, enabling the formation of a new droplet. The periodic oscillations in current and voltage throughout these phases are crucial in controlling the metal transfer and the arc stability for the GMAW-S process [22].

3.1.3 Analysis of waveform characteristics

Figures 8 and 9 demonstrate the effects of WFS , TS , and SG on the actual processing waveform characteristics (such as the mean current, power, and duration of each phase) of the CMT and GMAW-S tests, respectively, as compared with the preset values if applicable. Each data represents a mean value of measurements from several tests that have the

same processing parameter under assessment (see Table 1 for experimental details).

In the case of the CMT process, the actual duration of the boost phase rises with increased WFS , following closely with the preset value ($t_{b\text{-preset}}$) as shown in Fig. 8a; nonetheless, t_b remains constant with changing TS and SG . On the other hand, t_w and t_{sc} have not been preset in the CMT synergic program and change with the processing parameters (such as WFS , TS , and SG). t_w is governed by the time needed for the droplet to touch the weld pool; therefore, it is dependent on WFS , the melting rate of the electrode, and the diameter of the molten droplet. It can be observed that increased WFS and TS lead to decreased t_w (Fig. 8a). While the dependence of t_w on WFS is obvious, the decrease of t_w with increased TS may be due to a slight rise in arc intensity because the electrode interacts more with the substrate and less with the molten pool with increased TS .

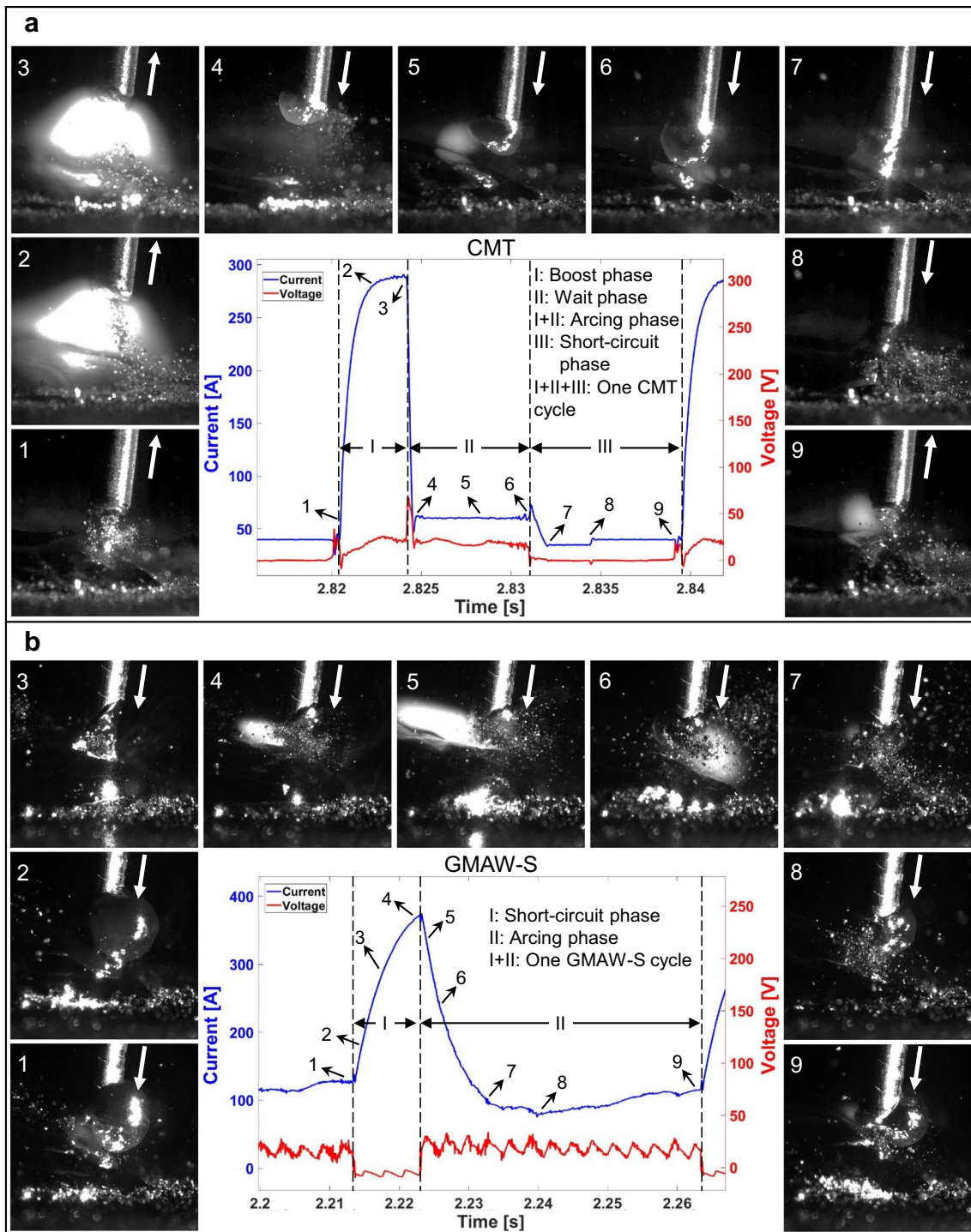


Fig. 7 A typical cycle of the current and voltage waveforms correlated with high-speed camera images at different moments as indicated along the waveform cycle: **a** CMT (a unit cycle including

phases I, II, and III) and **b** GMAW-S (a unit cycle including phases I and II). The white arrow indicates the direction of feed wire movement

CO_2 -containing SG mixtures lead to a slightly lower t_w as compared to O_2 -containing SG mixtures, which may be due to a higher burning rate in O_2 -containing SG mixtures. t_{sc} is the time interval needed for a droplet to detach as the feed

wire retracts, and its variation is negligible with changing WFS (Fig. 8a); it decreases as the TS increases, indicating that higher TS may mechanically promote the separation of the weld droplet with the molten pool. SG mixture does not

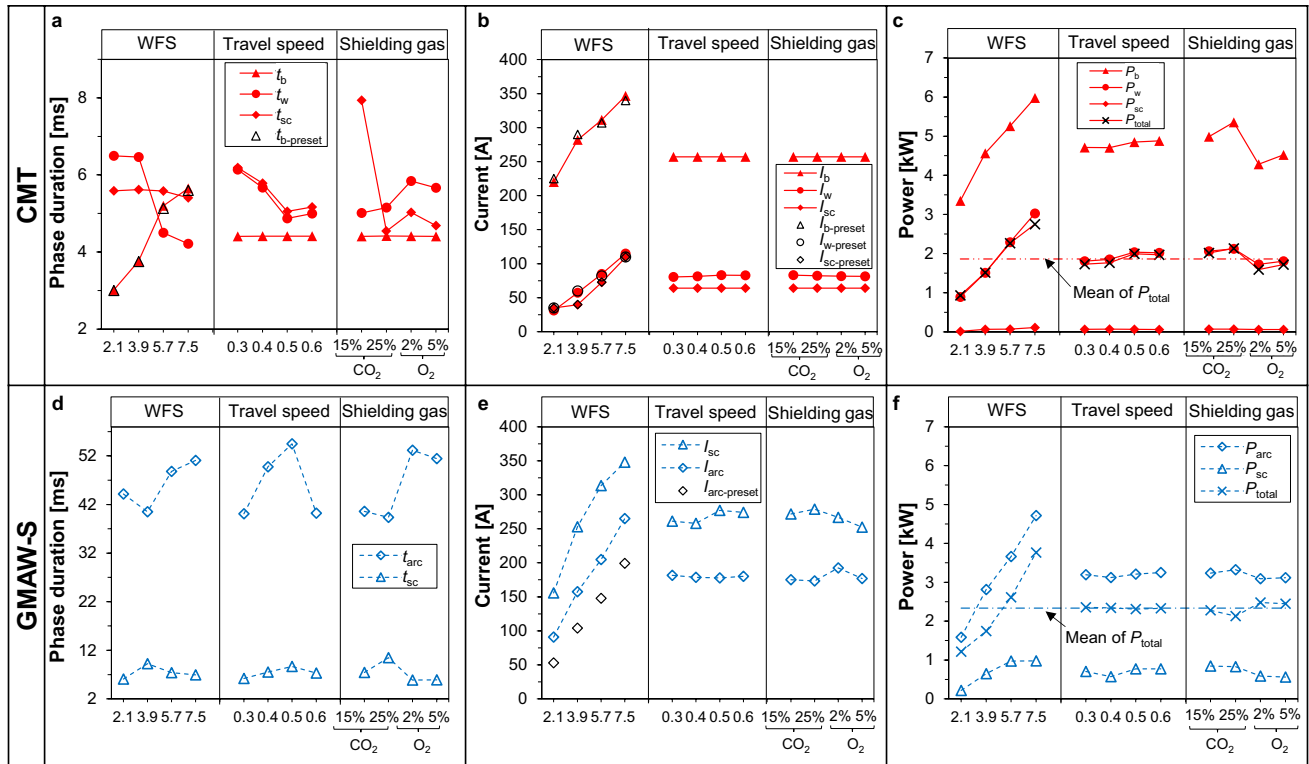


Fig. 8 Effects of processing parameters on the waveform characteristics of CMT and GMAW-S processes (a, d: mean of phase duration; b, e: current; c, f: power); horizontal dashed line indicates overall mean for total power

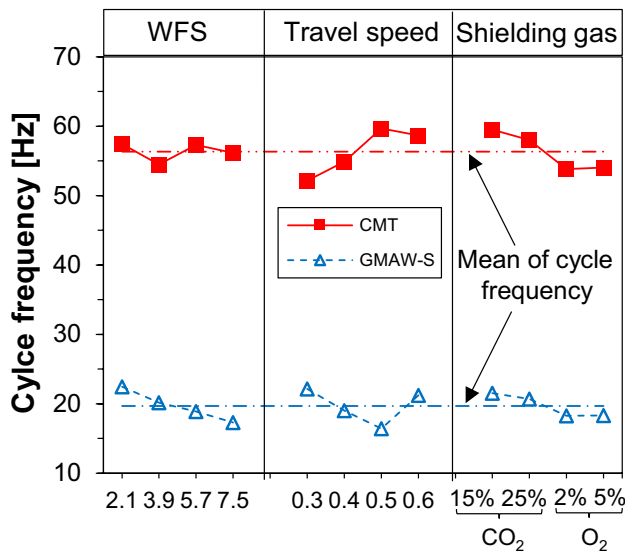


Fig. 9 Effects of processing parameters on the mean of cycle frequency for CMT and GMAW-S tests, respectively

seem to change t_{sc} much, with an exception for 15% CO_2 SG mixture where higher t_{sc} is observed.

In the case of GMAW-S, t_{arc} fluctuates significantly (Fig. 8d), suggesting lower stability compared to the CMT

tests. Although GMAW-S and CMT have different droplet detachment mechanisms, the range of their t_{sc} is comparable.

As shown in Fig. 9, the average cycle frequency for CMT is 56 Hz, which is much higher than that for GMAW-S (19 Hz). Fluctuation of the cycle’s frequency, ranging from 50 to 63 Hz, is small (less than $\pm 12\%$ from their mean) for CMT, whereas the fluctuation of cycle frequency for GMAW-S, ranging from 11 to 27 Hz (i.e., about $\pm 42\%$ from their mean), is much higher than that for CMT. This demonstrates the superior waveform stability of CMT as compared to GMAW-S.

In the case of CMT, I_b , I_w , and I_{sc} all increase with rising WFS closely following their preset values, and they are not affected by TS and SG (Fig. 8b), indicating great waveform stability for the CMT process at various processing conditions. Comparatively, for GMAW-S, actual processing I_{arc} also increases with rising WFS but is higher than the preset value (Fig. 8e). In addition, both I_{arc} and I_{sc} fluctuate slightly with changing TS and SG mixtures. All those are indications that the processing waveforms for GMAW-S are much more difficult to control and less stable, as compared to those for CMT. It is interesting to note that I_{arc} in GMAW-S is in the same range as I_b in the CMT tests. Nonetheless, I_{sc} for GMAW-S is much higher than that of CMT in a comparable processing condition, that is because a higher current is needed for the droplet detachment during the GMAW-S

process leading to higher arc instability, while the droplet detachment is facilitated by wire retraction at a lower current level for the CMT process leading to less spatter.

Consequently, the mean P_{sc} for CMT (varying from 15 to 122 W as shown in Fig. 8c) is much lower than that of GMAW-S (varying from 209 to 1198 W as shown in Fig. 8f) in a comparable processing condition. Although P_b for CMT is consistently greater than P_{arc} for GMAW-S across all tests, the total power for CMT is lower than that of GMAW-S, due to much shorter t_i than t_{arc} .

3.2 Physical loss of WC during deposition

In addition to WC dissolution, black residues containing WC particles were found along bead tracks of Ni-WC MMCs deposited by the CMT process, providing conclusive evidence that some WC particles were not caught up into the molten pool during deposition operation as reported in detail elsewhere [14]. Physical loss during the deposition process was also found to be one of the causes for reduced f_{WC} in similar weld overlays produced by the GMAW process with both short-circuit and globular transfer modes [23–25]. Guest et al. [24] determined the loss mechanism as the non-wetting behavior of WC particles. Utilizing high-speed camera images, they demonstrated that a portion of WC particles could not penetrate into the molten pool due to surface tension, either bouncing directly off or sitting on the molten pool surface before being further expelled by the welding arc.

Figure 10 shows high-speed camera images of typical CMT and GMAW-S tests, obtained during this investigation. It can be observed that some WC particles are blown away and wasted without having a chance to encounter the weld pool. This is different from the non-wetting behavior of WC particles as Guest et al. [24] documented before. For CMT, there are mainly two instances for the physical loss of WC particles: (1) during arc ignition and/or re-ignition (at the beginning of the boost phase) and (2) after the detachment of the molten droplet while retracting the electrode (as shown in Fig. 10a). For the former case, it may be due to excessive and uneven electromagnetic force during the arc initiation phase in association with the tubular electrode; for the latter case, particles within the open tubular sheath may fall out due to gravitational effect exacerbated by the feed wire retracting movement before the formation of the next droplet, and then blown away by flowing protective gas and electromagnetic force.

For GMAW-S, the loss of WC particles primarily occurs either during arcing phases especially at the current peaks or after droplet detachments leaving the tip of the tubular feed wire open. In addition, the molten droplet can be expelled away from the processing zone from the open side of the electrode (as clearly demonstrated in Fig. 10b). Because of cathode spot relocations which could often be the case,

especially for tubular electrodes [13], a weld droplet formed at the tip of the tubular feed wire can be attracted to one side at the tip, leaving another side of the electrode tip exposed and open from which WC particles are expelled away from the processing zone. This third type of physical losses is more prevalent for the GMAW-S process (which may be due to unstable arc), but can also be observed for the CMT process.

For the current investigation, the highest η achieved among all the tests is approximately 92.5% (see Table 2), indicating that physical loss of WC particles can be kept as low as 7.5% of the initial carbide amount in cored feed wire. For tests 1–4 of CMT and GMAW-S where the thermal input is at the lower range, low f_{WC} should be mainly due to physical losses, as WC dissolution is negligible; on that base, it can be reasonably assumed that physical loss can go as high as 44.5% of initial carbide amount in cored feed wire. Lower f_{WC} and η of CMT samples compared to GMAW-S ones with identical processing parameters (see the following subsection for details) can be attributed to the higher physical losses, due to more frequent events associated with detachments of molten droplets and arc re-initiations as well as exacerbated gravitational effects by wire-retracting actions for the CMT process. The increased cycle frequency (see Fig. 9) might lead to a larger physical loss of WC particles.

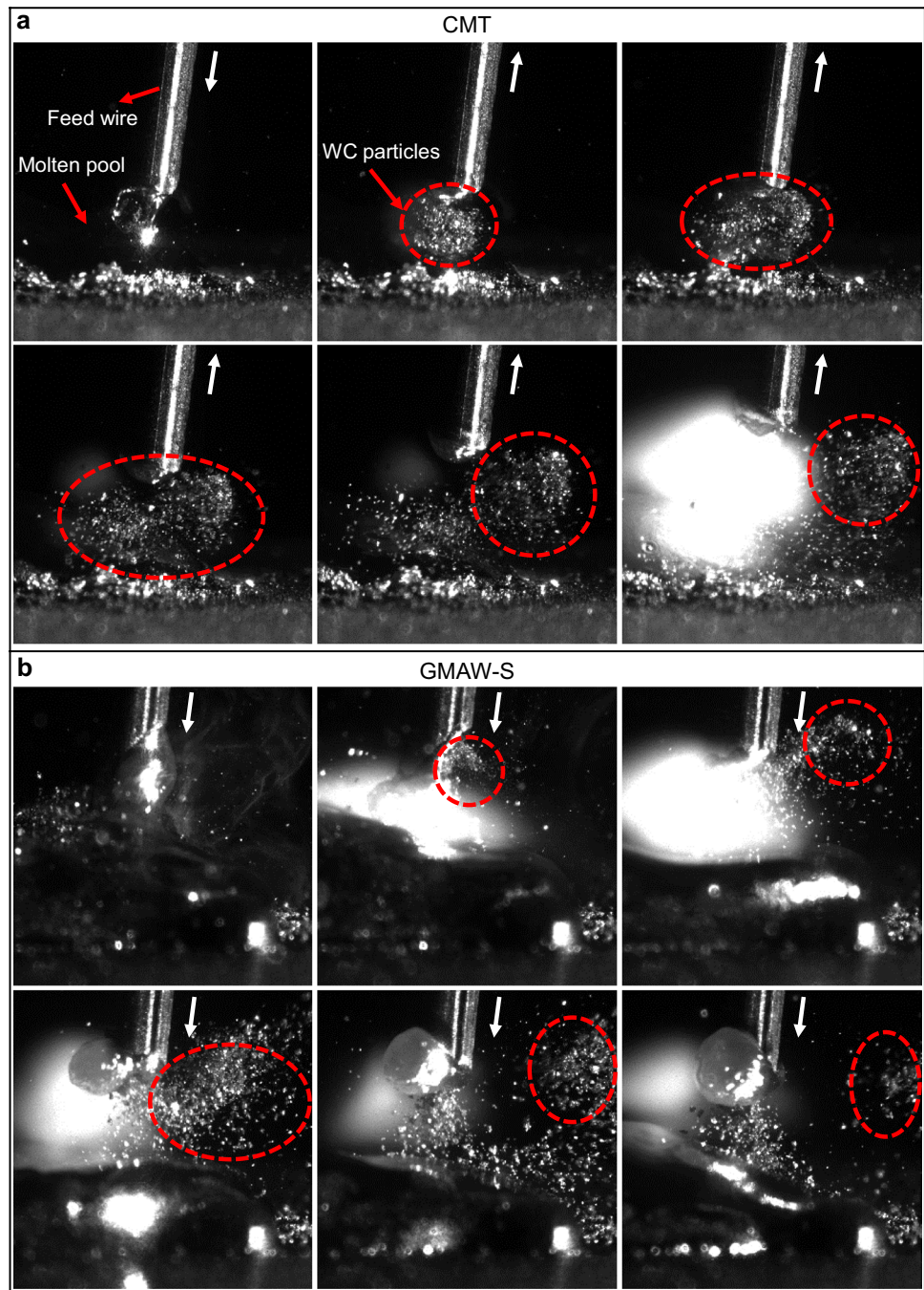
3.3 Effect of processing parameters on the overlay characteristics

Figure 11 presents the top view of CMT and GMAW-S bead tracks, respectively. Table 2 summarizes the experimental results regarding AIP , f_{WC} , η , dwell time, and characteristics of bead geometry. The bead profiles are continuous and relatively smooth, and bead surfaces are uniform without any noticeable defects or irregularities. These characteristics are crucial for cladding purposes where subsequent tracks can be deposited avoiding porosities. In tests 1–4 of CMT, the bead profiles are narrow which is not ideal for cladding applications. Low WFS causes insufficient arc power and feed wire melting, which reduces DR and results in lower deposition volumes.

Figure 12 exhibits the effects of WFS , TS , and SG on f_{WC} , η , and weld bead characteristics (DL , P , and W/H), respectively. Each data represents a mean value of measurements from several tests that have the same processing parameter to be assessed.

For CMT, it can be observed that increased WFS and TS lead to a decrease of f_{WC} and η . For GMAW-S, a similar trend is generally evident with the exception of WFS of 3.9 m/min, where there is a slight increase in f_{WC} and η compared to WFS of 2.1 m/min; this can be attributed to the low AIP for WFS of 2.1 m/min leading to an unstable arc and, thus, larger physical loss of WC particles.

Fig. 10 High-speed camera images indicating the physical loss of WC particles during deposition processes by **a** CMT and **b** GMAW-S. The time interval between the two adjacent frames is 2 ms for CMT and 4 ms for GMAW-S; the white arrow indicates the direction of feed wire movement



In general, higher WFS (which is related to higher processing current and AIP as discussed earlier) correlates with elevated arc intensity (and thus higher electromagnetic force) and higher HI , facilitating both physical loss of WC particles and WC dissolution in molten pools during the deposition process for both CMT and GMAW-S.

It is commonly believed that increased TS correlates with reduced HI and, thus, lower WC dissolution; this should lead to larger f_{WC} and η , a case that was observed previously with standard GAMW [5, 26]. Obviously, the outcomes of

the present study contradict this “common sense.” For current tests of the low- HI processes, the effect of physical loss (rather than that of carbide dissolution) may be predominant, which may be intensified with increased TS resulting in lower f_{WC} and η . In the case of the CMT process, it seems that both the cycle frequency of processing waveform and P_b in each cycle rise with increased TS , which may be the main cause of intensified physical loss of WC particles. For GMAW-S, P_{arc} in each cycle of the processing waveform seems to get slightly larger with increased TS , which may

Table 2 Summary of experimental results for CMT and GMAW-S processes

Test ID	AIP (kW)		f_{WC} (%)		η (%)		DL (%)		P (mm)		DR (kg/h)		W (mm)		H (mm)		A_R (mm ²)		Dwell time (s)	
	CMT	GMAW-S	CMT	GMAW-S	CMT	GMAW-S	CMT	GMAW-S	CMT	GMAW-S	CMT	GMAW-S	CMT	GMAW-S	CMT	GMAW-S	CMT	GMAW-S	CMT	GMAW-S
1	0.93	0.98	25.2	31.36	67.1	86.12	0.92	3.82	0.04	0.11	1.20	1.53	5.05	5.08	2.08	2.05	7.01	6.96	1.49	1.50
2	0.98	1.15	26.8	30.34	71.4	85.11	1.05	5.92	0.07	0.14	1.30	1.81	4.25	4.95	1.97	1.75	5.60	5.76	1.10	1.33
3	0.85	1.28	20.7	22.37	55.5	73.76	1.65	19.94	0.09	0.50	1.28	1.63	3.40	2.05	1.90	1.28	4.32	4.31	0.88	1.15
4	0.87	1.23	24.5	24.94	65.4	72.97	0.88	9.35	0.06	0.15	1.28	1.83	3.35	4.58	1.45	1.28	3.24	3.92	0.62	0.85
5	1.46	1.48	25.7	31.13	74.2	87.97	8.52	6.81	0.27	0.29	1.87	3.06	6.89	8.03	2.07	2.95	9.51	15.76	2.16	2.90
6	1.66	1.36	20.7	31.97	64.2	92.49	14.83	8.80	0.25	0.34	1.89	3.08	6.75	6.56	1.57	2.61	7.08	11.38	1.58	1.68
7	1.36	1.88	23.0	22.95	65.2	71.52	6.77	15.42	0.15	0.39	2.01	2.92	5.22	6.58	1.52	1.72	5.29	7.57	1.05	1.48
8	1.32	2.00	18.6	24.57	52.4	76.47	6.57	15.23	0.18	0.44	1.95	3.29	4.39	6.56	1.55	1.74	4.54	7.62	0.90	1.31
9	1.75	2.86	27.5	27.64	78.0	85.76	6.93	14.87	0.19	0.75	2.40	4.74	8.35	13.72	2.31	3.06	12.87	27.96	2.98	3.42
10	1.89	2.84	22.4	12.82	68.3	46.65	13.64	27.60	0.35	0.69	2.50	2.94	7.51	9.65	1.79	1.63	8.95	10.49	2.20	2.33
11	2.54	2.29	18.9	27.87	62.8	85.61	20.72	14.30	0.29	0.59	2.55	4.61	7.92	8.38	1.64	2.56	8.67	14.31	1.88	2.04
12	2.36	2.64	12.0	19.63	38.1	67.00	16.99	22.83	0.37	0.95	2.79	4.64	6.70	7.64	1.50	2.42	6.69	12.35	1.39	1.61
13	2.34	3.88	26.3	20.22	77.4	68.25	10.08	24.39	0.42	1.35	3.03	5.34	10.16	15.31	2.35	2.70	15.91	27.65	3.57	3.83
14	2.14	4.00	26.2	21.61	78.1	72.08	11.67	20.81	0.32	0.88	3.04	6.23	8.56	14.49	2.28	2.67	13.03	25.74	2.63	2.98
15	2.86	3.79	18.2	12.97	60.7	45.57	20.83	25.39	0.55	1.35	3.40	6.16	8.41	11.32	1.92	2.51	10.76	18.87	1.96	2.58
16	2.95	3.64	10.3	13.18	34.1	46.54	20.26	25.54	0.44	1.19	3.15	6.32	7.97	9.46	1.51	2.63	8.02	16.52	1.61	2.25

AIP average instantaneous power, f_{WC} volume fraction of retained WC, η carbide transfer efficiency, DL dilution level, P depth of penetration, DR deposition rate, W bead width, H bead height, A_R reinforcement area

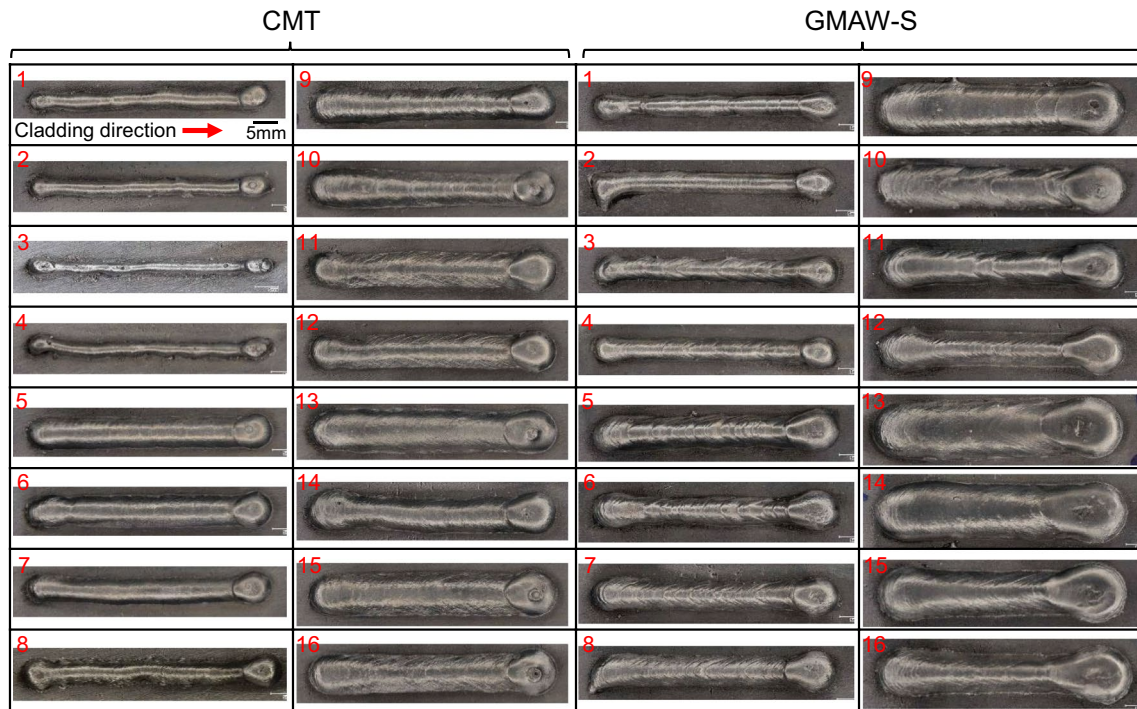


Fig. 11 Optical top-view images of bead tracks deposited by CMT and GMAW-S

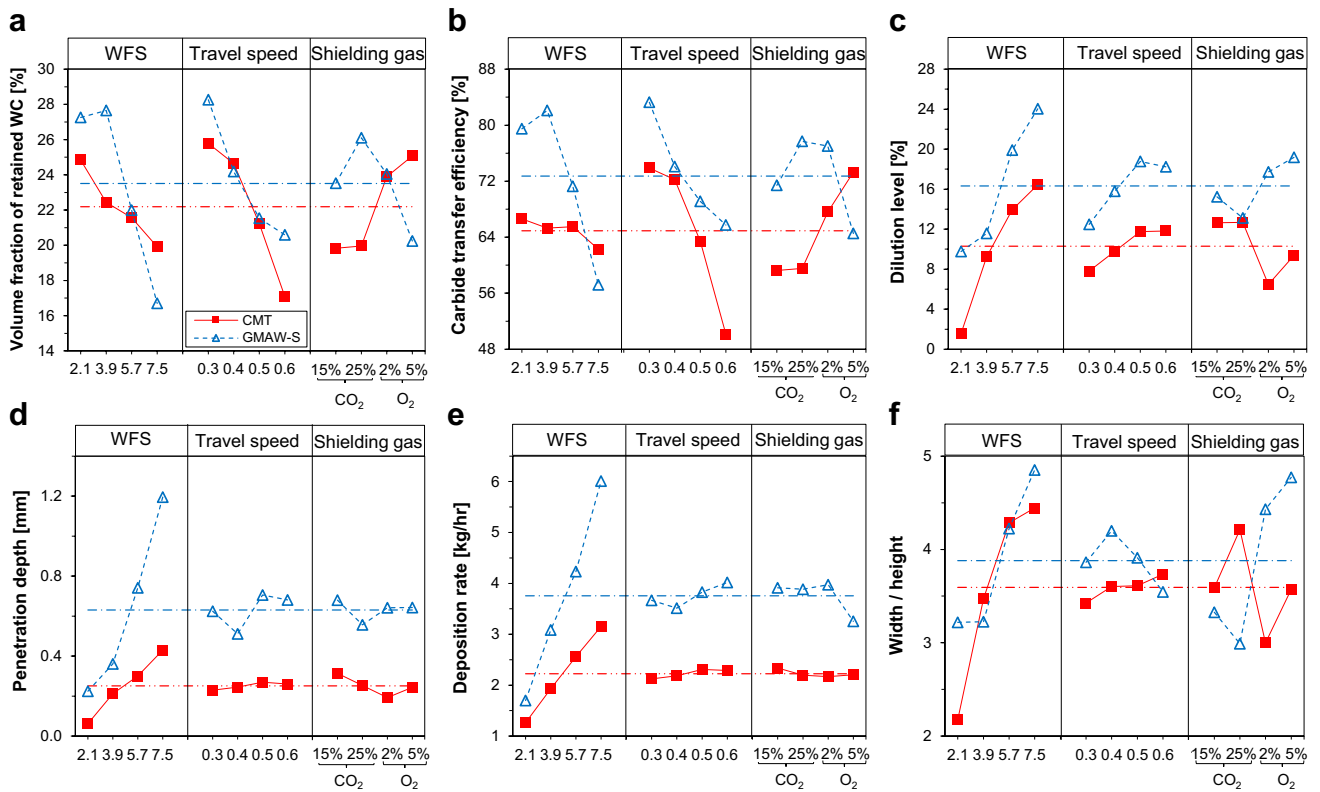


Fig. 12 Effects of processing parameters on the quality of the resultant overlays deposited by CMT and GMAW-S, respectively: **a** volume fraction of retained WC, **b** carbide transfer efficiency, **c** dilution level,

d penetration depth, **e** deposition rate, and **f** bead width-to-height ratio. Horizontal dashed lines indicate the overall means of corresponding parameters

be one contributing factor to the increased physical loss. In addition, with increasing TS , the arc intensity could be strengthened even at the same power level, because the electrode interacts more with the substrate and less with the molten pool, which may also promote the physical loss of WC particles during the deposition process.

For the CMT tests, CO_2 content in the SG mixture does not appear to significantly impact f_{WC} and η ; however, an increasing trend in f_{WC} and η is observed with the increasing level of O_2 in the SG mixture, which may be a reflection of the fact that O_2 addition results in lower waveform cycle frequency and P_b leading to lower physical loss of WC particles during the deposition process. Guest et al. [24] observed improvements in η with the addition of up to 15% O_2 for GMAW processes with both short-circuit and globular transfer modes. Introducing a controlled amount of oxidizing gas, such as CO_2 or O_2 , to an Ar-rich SG mixture can alter the thermophysical characteristics of the plasma arc, enhancing welding arc stability, heat transfer, surface tension, and weldability [27–29]. However, in the case of CMT, CO_2 addition to the SG appears to be less effective in achieving arc stability as compared to O_2 addition for depositing the Ni-WC material system. Molten nickel is resistant to oxidation, which results in fewer electron emissions and reduced stability at the cathodic locations. The presence of O_2 in SG effectively promotes the oxidation of the nickel weld pool and improves arc stability during the droplet formation [25]. Improved arc stability leads to less physical loss of carbides and increased η and higher f_{WC} .

For GMAW-S, in contrast, a higher level of CO_2 in the SG mixture increases f_{WC} and η , whereas the increase of O_2 content to 5% lowers f_{WC} and η although 2% O_2 seems to have a negligible effect. To that end, more studies are still needed to have a full understanding.

For both CMT and GMAW-S, WFS is the primary factor influencing weld bead characteristics and DR (see Fig. 12c–f). Higher WFS leads to an increase in AIP , resulting in greater substrate melting (directly increasing P , DL , and W/H).

Higher TS also increases DL , but its effect on the DR , P , and W/H remains either marginal or inconclusive for both CMT and GMAW-S. The effect of TS on bead geometrical characteristics is dependent on two combined effects of HI and arc impingement, which compete with each other [30, 31] as also discussed in our previous work [14].

The effect of the SG mixture on DL for CMT seems to be also different from that for GMAW-S. For CMT, DL remains almost unchanged when using SG mixture with CO_2 addition; however, O_2 addition results in relatively lower DL . In contrast, O_2 addition results in relatively higher DL for GMAW-S. Furthermore, O_2 addition in the SG mixture seems to result in lower W/H as compared with those with CO_2 addition for CMT, whereas lower levels of W/H seem to

be the case for GMAW-S with CO_2 -containing SG mixtures. SG compositions do not have a significant effect on the DR , except for slightly lower values for GMAW-S with 5% O_2 .

Figure 13 illustrates the effect of AIP on the quality criteria of all individual overlays. There is no strong correlation between f_{WC} or η and AIP . However, a subtle decreasing trend can be observed as AIP increases for both CMT and GMAW-S. As shown in Fig. 13, DR , dwell time, DL , P , A_R , W , H , and W/H show in general a positive correlation with AIP .

Interestingly, GMAW-S and CMT results in terms of AIP suggest no superiority of CMT over GMAW-S, except for better control in P , and slightly lower DL . Overall, GMAW-S may even slightly outperform CMT with respect to f_{WC} , η , and DR . W of the overlays shows comparable results and positive correlation with AIP for both CMT and GMAW-S tests. However, the impact of AIP is less profound on H . For instance, W of samples varies between 3.35–10.16 mm for CMT and 2–15.3 mm for GMAW-S, while H of samples varies only between 1.45–2.35 mm for CMT and between 1.3–3.1 mm for GMAW-S, respectively. In other words, higher AIP contributes to a higher melting rate of the electrode which mostly leads to wider beads rather than increasing bead height.

3.4 Microstructure and microhardness

CMT and GMAW-S test IDs 3, 7, 10, and 16, respectively, were selected to investigate the effect of processing parameters on the microstructure and microhardness of the overlays. The corresponding AIP for these tests is 0.85, 1.36, 1.89, and 2.95 kW for CMT and 1.28, 1.88, 2.84, and 3.64 kW for GMAW-S, respectively. Figure 14 shows the micrographs of these samples with EDS measurements for Fe and Ni.

A previous paper by the authors [14] extensively characterized the microstructure of CMT samples which consisted of the retained WC fairly uniformly distributed within the matrix of γ -Ni and eutectic Ni/Ni₃B. Degradation seams are not observed around the retained WC particles. They exhibit an excellent metallurgical bond with the adjacent matrix. Nevertheless, WC particles inevitably experience partial dissolution in the molten pool, leading to an increased concentration of W in the Ni-based matrix. Accordingly, primary WC precipitates can be seen in all the overlay samples. As indicated by the EDS results presented in Fig. 14, the concentration of W (tungsten) increases toward the top of the overlay, possibly due to the effect of partially directional solidification starting from the interface with the substrate and due to the longer dwell time of WC in liquid metal at the upper portion of an overlay (increasing the likelihood of WC dissolution).

For CMT samples, secondary carbides are also observed in the form of W_2C and/or W-rich carbides for tests with AIP smaller than 1.9 kW and in the form of M_6C (Ni₂W₄C near the top and Fe₃W₃C closer to the interface) for those with

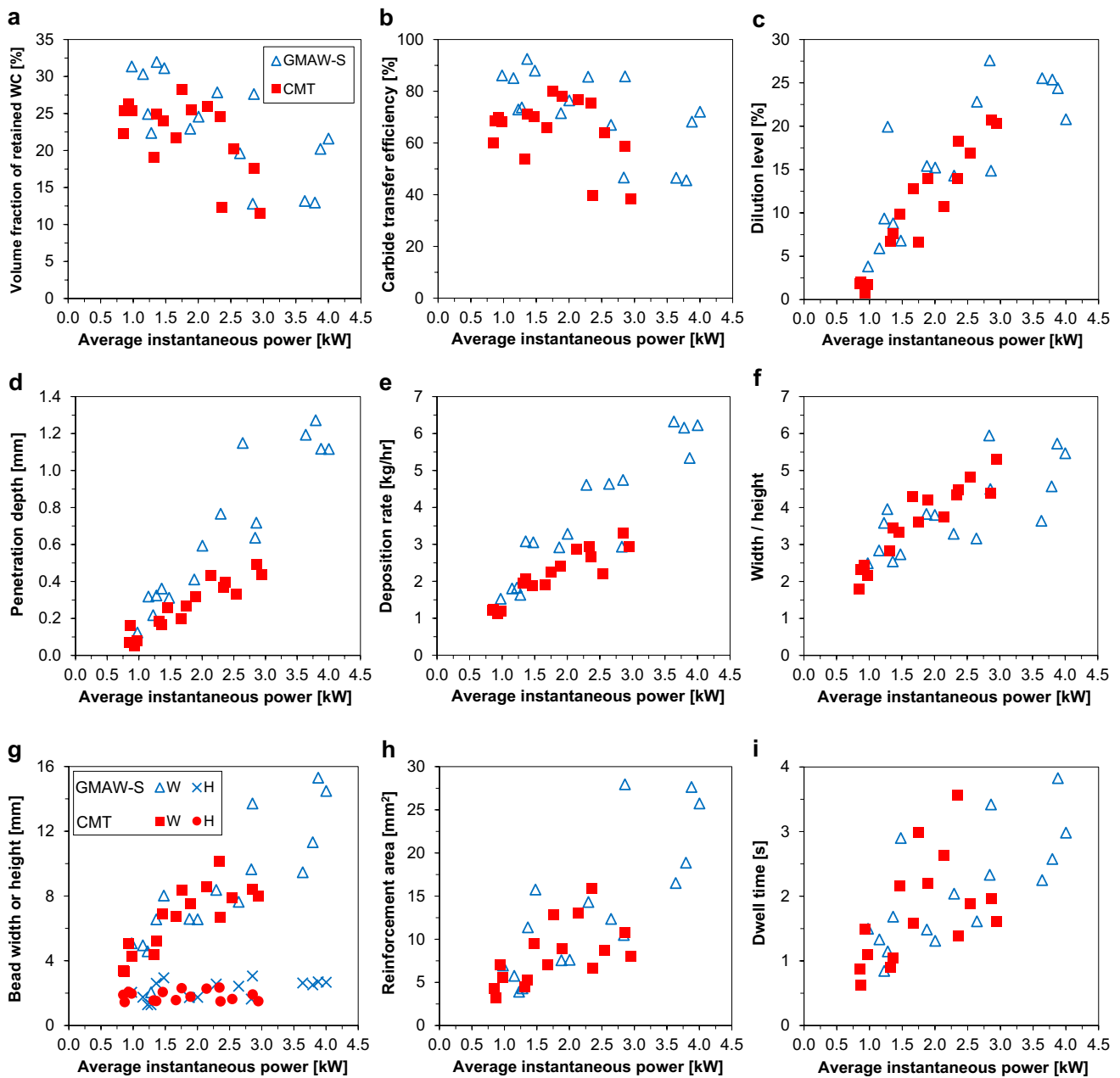


Fig. 13 Effects of average instantaneous power on quality criteria of the overlays deposited by CMT and GMAW-S: **a** volume fraction of retained WC, **b** carbide transfer efficiency, **c** dilution level, **d** pene-

tration depth, **e** deposition rate, **f** bead width-to-height ratio, **g** bead width or height, **h** the reinforcement area of an overlay bead, and **i** dwell time of WC in the molten pool

AIP greater than 2 kW, respectively. Fe enters into an overlay due to dilution and, consequently, higher content of Fe in the matrix closer to the interface can be measured.

For GMAW-S samples, secondary carbides in the form of W_2C , W-rich carbides, and/or M_6C can be observed in all the tests. The major difference in the microstructure is the formation of herringbone carbides near the interface of GMAW-S samples at lower AIP (i.e., even for a microstructure-examined sample with the lowest AIP of 1.28 kW),

while the same carbide is only observed at relatively higher AIP (greater than 1.89 kW) for CMT samples. This can be attributed to a higher concentration of Fe in the matrix due to elevated DL for GMAW-S specimens (as confirmed by EDS results shown in Fig. 14b) as compared to CMT ones, which facilitates the precipitation of secondary carbides (such as Fe_3W_3C) in GMAW overlays.

CMT samples exhibit higher W concentration and lower Fe concentration, as compared with GMAW-S ones

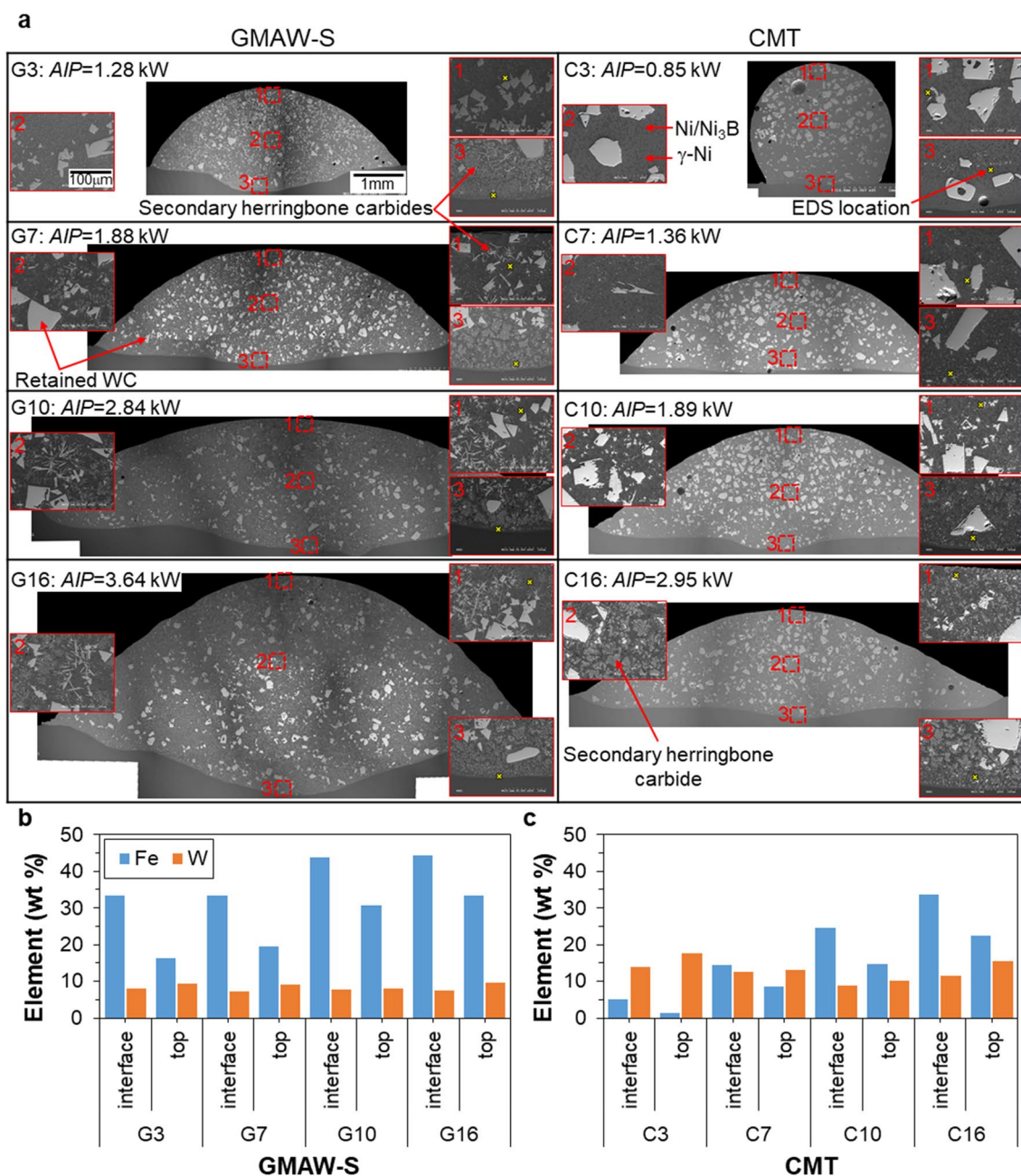


Fig. 14 Backscattered-electron images of tests 3, 7, 10, and 16 for GMAW-S and CMT, respectively, with marked locations for EDS measurements (a); EDS spot measurement results of Fe and W in the overlay matrix at marked locations (b: GMAW-S; and c: CMT)

with comparable AIP (i.e., GMAW-S samples 3, 7, and 10 versus CMT samples 7, 10, and 16, respectively). A possible explanation is that, for GMAW-S specimens, W is being consumed in the precipitation of secondary carbides (such as Fe_3W_3C) promoted by higher DL , leaving the matrix with less W concentration after solidification.

Figure 15 shows indentation marks across the centerline of the overlays' cross-section and their average

values. As references, the hardness of the tubular Ni-sheath and the substrate was measured, with the average value being about 202 and 218 $HV_{0.5}$, respectively.

By avoiding large WC particles, the measured microhardness is most related to the matrix. That is in line with the fact that no cracks were observed around the majority of the Vickers indentations and that cracks can only be seen occasionally (in the matrix or when smaller WC particles were being pressed by the indenter).

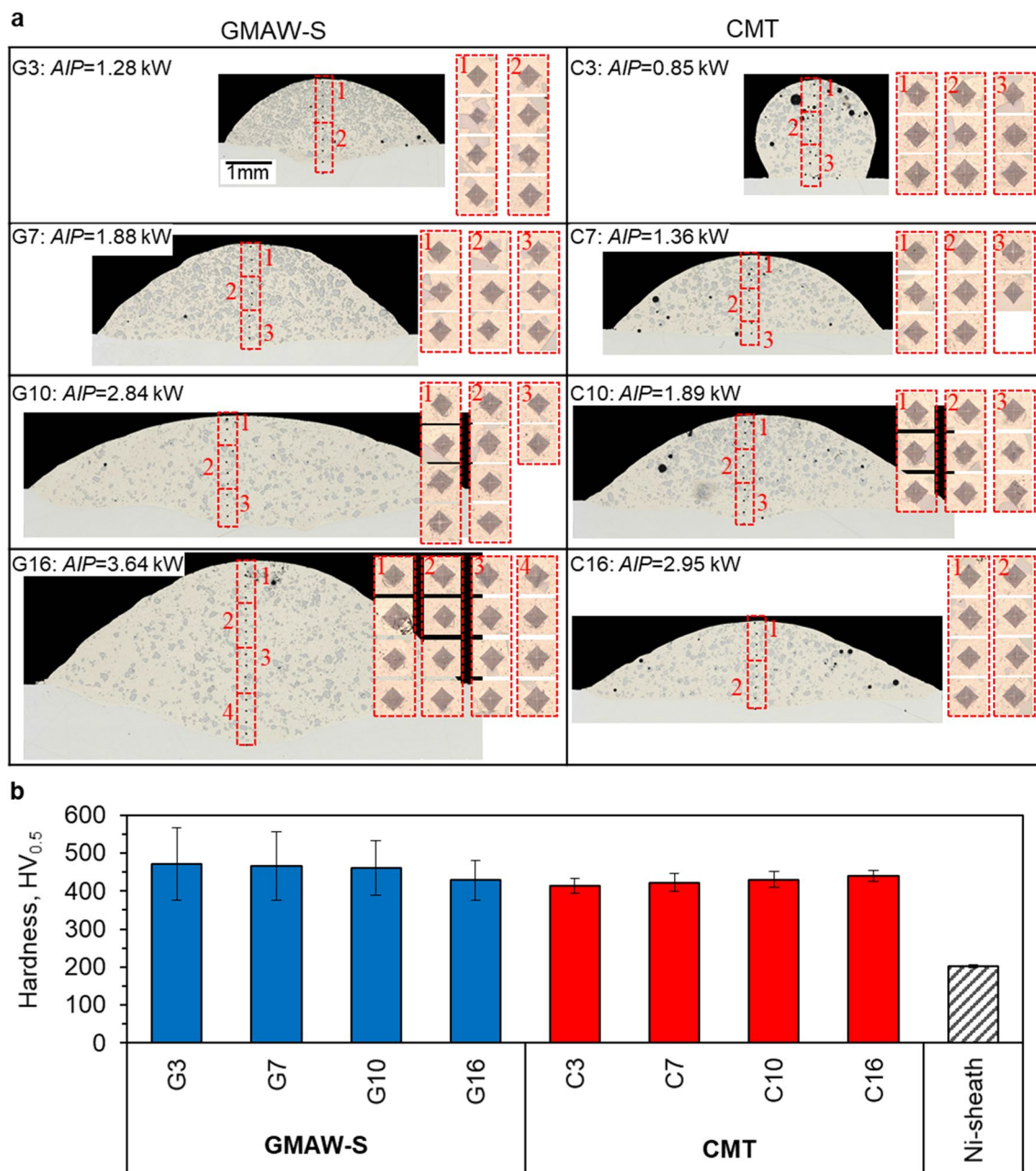


Fig. 15 Microhardness measurements of overlays deposited during tests 3, 7, 10, and 16 for GMAW-S and CMT, respectively: **a** microhardness indentation marks across the centerlines of the overlay cross-sections and **b** the average microhardness values of the overlays

The large variations of the hardness numbers can be partially due to the interactions of the indenter with small secondary carbides (or occasionally even with larger primary WC), especially for GMAW-S samples where secondary carbides are more predominant. The much higher hardness of the matrix than the nickel sheath is attributed to a combination of several factors, such as solid solution strengthening (by alloy elements, such as

Si and B contained in the core of the feed wire as well as W and Fe mixing into the substrate during the deposition process), dispersion strengthening mechanism [31] (e.g., associated with small secondary carbides), and grain refinement strengthening [32] (i.e., grain refinement due to the presence of retained and primary carbides).

In general, microhardness values of GMAW-S samples are slightly higher than that of CMT ones with roughly

comparable *AIP* values. This may be attributed to the fact that there is a higher volume fraction of secondary carbide precipitates in the matrix of a GMAW-S sample compared to a comparable CMT one.

4 Conclusions

Short-circuit GMAW processes with/without mechanically assisted droplet transfer (i.e., CMT vs. GMAW-S) have been investigated for depositing Ni-WC MMC overlays, leading to the following conclusions:

- In contrast to common expectations, advanced CMT technology could not demonstrate significant advantages over GMAW-S; on the contrary, GMAW-S exhibits marginal advantages over CMT in terms of carbide transfer efficiency, volume fraction of retained WC, and deposition rate.
- Some carbides contained in the core of the feed wire are blown away and expelled out of the processing zone: (1) during arcing phase, especially at arc ignition and/or re-ignition stages, due to excessive and uneven electromagnetic force; (2) owing to particles dropping out of the open tip of the tubular feed wire (due to gravitational effect) after the detachment of a molten droplet (and then blown away); and (3) from local opening (due to a weld droplet unevenly attached to the tip of the tubular feed wire). The first two mechanisms prevail for the CMT process.
- The physical loss of WC particles is more significant for the CMT process owing to much higher waveform cycle frequency and cyclic feed wire retractions, despite superior waveform stability and better control over penetration depth, marginally lower dilution level, and exceptional arc stability.
- Cyclograms indicate that the CMT process has greater process stability, higher data consistency, and lower data noise, while the GMAW-S process exhibits a lack of regularity, lower process stability, and greater data scattering and noise.
- For both processes, the carbide transfer efficiency and the volume fraction of retained WC are generally negatively correlated with the wire feed rate and the travel speed.
- For GMAW-S tests, the higher level of CO₂ in shielding gas mixture improves the carbide transfer efficiency and the volume fraction of retained WC, whereas the addition of O₂ in shielding gas demonstrates the same effect for CMT.
- The microstructural characteristics of CMT and GMAW-S overlays are mostly similar. CMT overlays

exhibit comparatively higher W but lower Fe concentration in the matrix. Herringbone-like M₆C secondary carbide precipitates are more prevalent in GMAW-S overlays, supposedly due to an elevated dilution level.

- GMAW-S overlays demonstrate marginally higher matrix microhardness.

Glossary *AIP* Average instantaneous power

A_P	Area of weld penetration
A_R	Reinforcement area of a weld bead
A_{WC}	Total area of WC particles
BSE	Backscattered electrons
CMT	Cold metal transfer
<i>DL</i>	Dilution level
DOE	Design of experiments
<i>DR</i>	Deposition rate
EDS	Energy-dispersive X-ray spectrometer
f_p	Initial volume fraction of carbide particles in cored feed wire
f_{WC}	Volume fraction of retained WC
GMAW	Gas metal arc welding
GMAW-S	GMAW with short-circuit metal transfer mode
η	Carbide transfer efficiency
<i>H</i>	Height of weld bead
<i>HI</i>	Heat input
<i>I</i>	Current
I_{arc}	Arcing current in GMAW-S
I_b	Boost current in CMT
I_{sc}	Short-circuit current in CMT or GMAW-S
I_w	Wait current in CMT
l_m	Linear mass of the electrode
Ni-WC MMC	Nickel-based metal matrix composites reinforced with WC
<i>P</i>	Penetration depth
P_{arc}	Arcing power in GMAW-S
P_b	Boost power in CMT
P_{sc}	Short-circuit power in CMT/GMAW-S
P_w	Wait power in CMT
SEM	Scanning electron microscopy
<i>SG</i>	Shielding gas
t_{arc}	Duration of arc phase in GMAW-S
t_b	Duration of boost phase in CMT
t_{sc}	Duration of short-circuit phase in CMT or GMAW-S
t_w	Duration of wait phase in CMT
<i>TS</i>	Travel speed
<i>V</i>	Voltage
<i>W</i>	Width of a weld bead
<i>W/H</i>	Width-to-height ratio of a weld bead
WC	Mono-crystalline tungsten carbide
<i>WFS</i>	Wire feed speed

Acknowledgements The authors are grateful to the Energy, Mining and Environment Research Centre, the National Research Council of Canada, for providing the required materials, facilities, and technical support for the experimental work.

Funding Open Access funding provided by National Research Council of Canada. This work is funded by the CWB Welding Foundation, the National Research Council of Canada, and the Natural Sciences and Engineering Research Council of Canada.

Data availability Not applicable.

Code availability Not applicable.

Declarations

Ethics approval Not applicable.

Consent to participate Not applicable.

Consent for publication Not applicable.

Conflict of interest The authors declare no competing interests.

Open Access This article is licensed under a Creative Commons Attribution 4.0 International License, which permits use, sharing, adaptation, distribution and reproduction in any medium or format, as long as you give appropriate credit to the original author(s) and the source, provide a link to the Creative Commons licence, and indicate if changes were made. The images or other third party material in this article are included in the article's Creative Commons licence, unless indicated otherwise in a credit line to the material. If material is not included in the article's Creative Commons licence and your intended use is not permitted by statutory regulation or exceeds the permitted use, you will need to obtain permission directly from the copyright holder. To view a copy of this licence, visit <http://creativecommons.org/licenses/by/4.0/>.

References

- Fisher G, Wolfe T (2013) Protective overlays and coatings used in oil sands. In: Tucker RC Jr (ed) Thermal spray technology. ASM International, pp 312–317
- Rojas JGM, Ghasri-Khouzani M, Wolfe T et al (2021) Preliminary geometrical and microstructural characterization of WC-reinforced NiCrBSi matrix composites fabricated by plasma transferred arc additive manufacturing through Taguchi-based experimentation. *Int J Adv Manuf Technol* 113:1451–1468. <https://doi.org/10.1007/s00170-020-06388-2>
- Mendez PF, Barnes N, Bell K et al (2014) Welding processes for wear resistant overlays. *J Manuf Process* 16:4–25. <https://doi.org/10.1016/j.jmapro.2013.06.011>
- Barnes N, Joseph T, Mendez PF (2015) Issues associated with welding and surfacing of large mobile mining equipment for use in oil sands applications. *Science and Technology of Welding and Joining* 20:483–493. <https://doi.org/10.1179/1362171815Y.0000000060>
- Günther K, Bergmann JP (2021) Experimental approach to determine the impact of the droplet transfer mode on the degradation of fused tungsten carbides during GMAW. *Int J Refract Met Hard Mater* 101:105692. <https://doi.org/10.1016/j.ijrmhm.2021.105692>
- Cornacchia G, Cecchel S, Panvini A (2018) A comparative study of mechanical properties of metal inert gas (MIG)-cold metal transfer (CMT) and fiber laser-MIG hybrid welds for 6005A T6 extruded sheet. *Int J Adv Manuf Technol* 94:2017–2030. <https://doi.org/10.1007/s00170-017-0914-9>
- Gungor B, Kaluc E, Taban E, Sik ŞŞA (2014) Mechanical and microstructural properties of robotic cold metal transfer (CMT) welded 5083-H111 and 6082-T651 aluminum alloys. *Mater Des*. <https://doi.org/10.1016/j.matdes.2013.08.018>
- Singh J, Singh Arora K, Kumar Shukla D (2020) High cycle fatigue performance of cold metal transfer (CMT) brazed C-Mn-440 steel joints. *Int J Fatigue* 137:105663. <https://doi.org/10.1016/j.ijfatigue.2020.105663>
- Cao R, Feng Z, Chen JH (2014) Microstructures and properties of titanium-copper lap welded joints by cold metal transfer technology. *Mater Des* 53:192–201. <https://doi.org/10.1016/j.matdes.2013.06.030>
- Zhou S, Xie H, Ni J et al (2022) Metal transfer behavior during CMT-based wire arc additive manufacturing of Ti-6Al-4V alloy. *J Manuf Process* 82:159–173. <https://doi.org/10.1016/j.jmapro.2022.07.063>
- Lehmann T, Jain A, Jain Y et al (2020) Concurrent geometry- and material-based process identification and optimization for robotic CMT-based wire arc additive manufacturing. *Mater Des* 194:108841. <https://doi.org/10.1016/j.matdes.2020.108841>
- Galeazzi D, Gonçalves e Silva RH, Viviani AB et al (2022) Evaluation of thermal and geometric properties of martensitic stainless steel thin walls built by additive manufacturing cold metal transfer (CMT) processes. *Int J Adv Manuf Technol*. <https://doi.org/10.1007/s00170-022-08921-x>
- Scott KM (2011) Heat transfer and calorimetry of tubular Ni / WC wires deposited with GMAW. University of Alberta
- Karimi MR, Wang S-H, Jelovica J (2022) Taguchi-based experimental investigation into weld cladding of Ni-WC MMC overlays by CMT process. *Int J Adv Manuf Technol* 122:2433–2461. <https://doi.org/10.1007/s00170-022-09816-7>
- COR@FACE 164 MC datasheet. <http://www.cor-met.com/products/hardfacing>. Accessed 13 Apr 2022
- Joseph A, Harwig D, Farson DF, Richardson R (2003) Measurement and calculation of arc power and heat transfer efficiency in pulsed gas metal arc welding. *Science and Technology of Welding and Joining* 8:400–406. <https://doi.org/10.1179/136217103225005642>
- Pepe N, Egerland S, Colegrove PA et al (2011) Measuring the process efficiency of controlled gas metal arc welding processes. *Science and Technology of Welding and Joining* 16:412–417. <https://doi.org/10.1179/1362171810Y.0000000029>
- Arevalo HDH, Vilarinho LO (2012) Desenvolvimento e avaliação de calorímetros por nitrogênio líquido e fluxo contínuo para medição de aporte térmico. *Soldag Inspeção* 17:236–250. <https://doi.org/10.1590/S0104-92242012000300008>
- Kumar M, Quadir Moinuddin S, Kumar SS, Sharma A (2021) Discrete wavelet analysis of mutually interfering co-existing welding signals in twin-wire robotic welding. *J Manuf Process* 63:139–151. <https://doi.org/10.1016/j.jmapro.2020.04.048>
- Ribeiro RA, Assunção PDC, Gerlich AP (2021) Suppression of arc wandering during cold wire-assisted pulsed gas metal arc welding. *Weld World* 65:1749–1758. <https://doi.org/10.1007/s40194-021-01155-7>
- Chen M, Zhang D, Wu C (2017) Current waveform effects on CMT welding of mild steel. *J Mater Process Technol* 243:395–404. <https://doi.org/10.1016/j.jmatprotec.2017.01.004>
- Gonçalves e Silva RH, Galeazzi D, Rocha PCJ et al (2021) Multiple output analysis for advanced waveform and controlled short-circuit MIG/MAG variants. *Weld World* 65:2267–2282. <https://doi.org/10.1007/s40194-021-01176-2>
- Günther K, Liefeth J, Henckell P et al (2018) Influence of processing conditions on the degradation kinetics of fused tungsten carbides in hardfacing. *Int J Refract Met Hard Mater* 70:224–231. <https://doi.org/10.1016/j.ijrmhm.2017.10.015>

24. Guest SD, Chapuis J, Wood G, Mendez PF (2014) Non-wetting behaviour of tungsten carbide powders in nickel weld pool: new loss mechanism in GMAW overlays. *Science and Technology of Welding and Joining* 19:133–141. <https://doi.org/10.1179/1362171813Y.0000000178>
25. Guest SD (2014) Depositing Ni-WC wear resistant overlays with hot-wire assist technology. University of Alberta
26. Wong Y-R, Ling S-F (2014) An investigation of dynamical metal transfer in GMAW—effects of argon shielding gas. *J Mater Process Technol* 214:106–111. <https://doi.org/10.1016/j.jmatprotec.2013.08.003>
27. Bitharas I, McPherson NA, McGhie W et al (2018) Visualisation and optimisation of shielding gas coverage during gas metal arc welding. *J Mater Process Technol* 255:451–462. <https://doi.org/10.1016/j.jmatprotec.2017.11.048>
28. Wang LL, Lu FG, Wang HP et al (2014) Effects of shielding gas composition on arc profile and molten pool dynamics in gas metal arc welding of steels. *J Phys D Appl Phys* 47. <https://doi.org/10.1088/0022-3727/47/46/465202>
29. Silva CC (2013) Weld overlay BT - encyclopedia of tribology. In: Wang QJ, Chung Y-W (eds) Springer. US, Boston, MA, pp 4094–4101
30. Näkki J (2018) Properties of alloy 625 claddings made with laser and CMT methods. Tampere University of Technology
31. Zhao S, Xu S, Huang Y, Yang L (2021) Laser hot-wire cladding of Ni/WC composite coatings with a tubular cored wire. *J Mater Process Technol* 298:117273. <https://doi.org/10.1016/j.jmatprotec.2021.117273>
32. Xiao Q, Sun WL, Yang KX et al (2021) Wear mechanisms and micro-evaluation on WC particles investigation of WC-Fe composite coatings fabricated by laser cladding. *Surf Coat Technol* 420:127341. <https://doi.org/10.1016/j.surfcoat.2021.127341>

Publisher's note Springer Nature remains neutral with regard to jurisdictional claims in published maps and institutional affiliations.